Geophysical Journal International

Geophys. J. Int. (2023) **233,** 1694–1707
Advance Access publication 2022 December 26
GJI Gravity, Geodesy and Tides

https://doi.org/10.1093/gji/ggac512

The 2021 M_W 6.2 Mamuju, West Sulawesi, Indonesia earthquake: partial rupture of the Makassar Strait thrust

Irwan Meilano [1], Rino Salman,[2] Susilo Susilo,[3] Hasbi Ash Shiddiqi [4], Pepen Supendi [5,6] Karen Lythgoe [2], Cheryl Tay,[7] Kyle Bradley,[2] Suchi Rahmadani,[1,8] Said Kristyawan[5] and Sang-Ho Yun[2,7,9]

[1] *Faculty of Earth Sciences and Technology, Institute of Technology Bandung (ITB), Bandung* 40132, *Indonesia. E-mail: irwanm@itb.ac.id*
[2] *Earth Observatory of Singapore, Nanyang Technological University, Singapore* 639798, *Singapore*
[3] *National Agency for Research and Innovation (BRIN), Cibinong Bogor* 16911, *Indonesia*
[4] *Department of Earth Science, University of Bergen, Bergen N-5020, Norway*
[5] *Agency for Meteorology, Climatology, and Geophysics (BMKG), Jakarta* 10720, *Indonesia*
[6] *Department of Earth Sciences, University of Cambridge, Cambridge CB*2 3*EQ, UK*
[7] *Asian School of the Environment, Nanyang Technological University, Singapore* 639798, *Singapore*
[8] *Centre for Earthquake Science and Technology, Institute of Technology Bandung (ITB), Bandung* 40132, *Indonesia*
[9] *School of Electrical and Electronic Engineering, Nanyang Technological University, Singapore* 639798, *Singapore*

Accepted 2022 December 10. Received 2022 August 16; in original form 2022 February 7

SUMMARY

On the 2021 January 15 (local date), an M_W 6.2 earthquake struck the Mamuju and Majene regions of West Sulawesi, Indonesia. This event killed more than 100 inhabitants, leaving at least 30 000 people displaced from their homes, and damaged almost 8000 buildings within a radius of ∼30 km from the main shock's epicentre location (as shown on our damage proxy map). This event was generated by an active fault that continues to the Makassar Strait Thrust (MST) offshore West Sulawesi. The hazard potential of this fault remains poorly understood. In this study, we use seismic and Global Positioning System (GPS) data to investigate the source characteristics of the main shock. The results suggest that the main shock partially ruptured one segment of the MST, activated a secondary fault structure, and likely brought the updip unruptured section of the MST segment closure to failure. Our analysis of interseismic GPS velocities indicates that the Mamuju and Majene regions have a higher crustal strain rate than other nearby regions. The results (partial rupture of the MST segment, the updip unruptured section of the MST and high strain rate in the Mamuju and Majene regions) together suggest a significant seismic hazard potential in West Sulawesi, particularly in the Mamuju and Majene areas.

Key words: Radar interferometry; Space geodetic surveys; Waveform inversion; Earthquake hazards.

1 INTRODUCTION

Active faulting on the island of Sulawesi, eastern Indonesia, accommodates relative motion between at least four microblocks (Socquet *et al.* 2006; Simons *et al.* 2007), due to its location at the triple junction between the Philippine Sea, Sunda and Australia plates (Hamilton 1979). In Central Sulawesi, for example, the relative motion between the Makassar and the North Sula blocks is accommodated by the Palu-Koro strike-slip fault (Socquet *et al.* 2006) which generated the 2018 M_W 7.5 Sulawesi earthquake (Fig. 1). In West Sulawesi, the Makassar block marks the eastern boundary of the Sunda plate (Simons *et al.* 2007). The relative motion between the Makassar block and the Sunda plate is accommodated by the Makassar Strait Thrust (MST, Bergman *et al.* 1996; Puspita *et al.* 2005; Socquet *et al.* 2006) which has been divided into the Somba, the Mamuju (hereafter referred to as 'MSTM'), the Central (hereafter referred to as 'MSTC') and the North (hereafter referred to as 'MSTN') segments (Fig. 1, Irsyam *et al.* 2017). Whilst the slip rate of the MST is approximately one quarter that of the Palu-Koro fault (Socquet *et al.* 2006), the MST still presents earthquake hazards to population centres along the western coast of Sulawesi. The MST generated the 1969 M_W 7.0 Majene and the 1984 M_W 6.7 Mamuju earthquakes (Storchak *et al.* 2013, 2015; Di Giacomo *et al.* 2018, Fig. 1) within the last 100 yr; 64 people lost their lives due to the 1969 event (Prasetya *et al.* 2001). Recently, the MST ruptured during the 2021 January 15 M_W 6.2 Mamuju earthquake (Gunawan

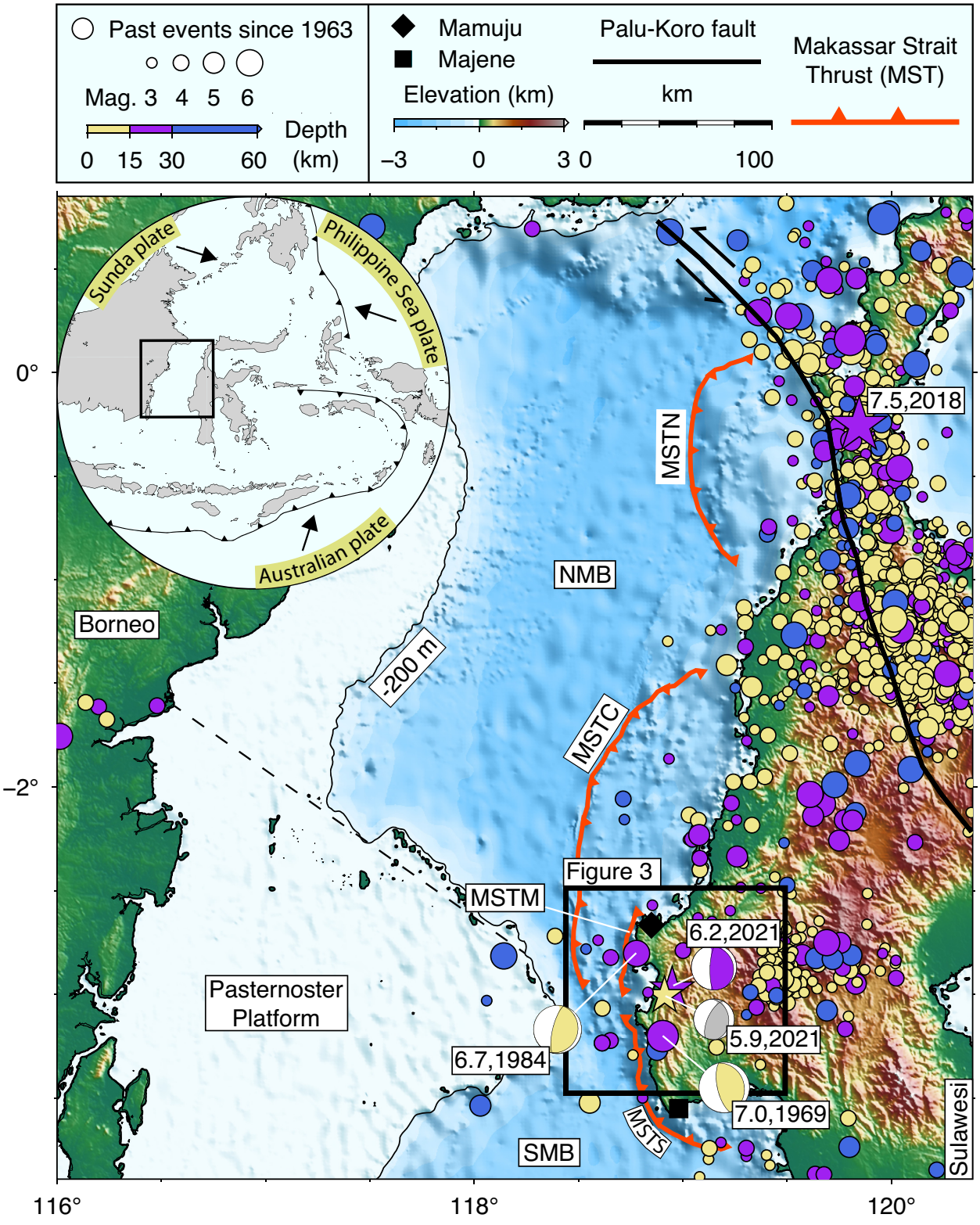

Figure 1. The 2021 January 15 M_W 6.2 Mamuju earthquake occurred near the active MST system and was preceded by foreshock events, the largest one was an M_W 5.9 earthquake. Before the Mamuju event, the recent largest earthquake was the 2018 M_W 7.5 event which ruptured the Palu-Koro fault ∼300 km to the northeast. The closest $M_W > 6$ earthquakes were the 1969 M_W 7.0 earthquake ∼25 km to the south–southwest and the 1984 M_W 6.7 earthquake ∼25 km to the northwest. Focal mechanisms for the M_W 6.2, M_W 5.9, M_W 7.0, M_W 6.7 events are from this work, the U.S. Geological Survey (USGS) earthquake catalogue, Fitch (1972) and the GCMT catalogue (Dziewonski *et al.* 1981; Ekström *et al.* 2012), respectively. Coloured circles represent earthquakes during 1963–2009 (Storchak *et al.* 2013, 2015; Di Giacomo *et al.* 2018), 2009–2018 (Supendi *et al.* 2019; Supendi *et al.* 2020) and 2018–2021 (USGS catalogue). The bathymetric high south of the NW-SE black dashed line is the Paternoster Platform, which is bounded by the North Makassar Basin (NMB) and the South Makassar Basin (SMB, Puspita *et al.* 2005; Hall 2011). The inset figure shows that Sulawesi is located within the triple junction of three tectonic plates.

et al. 2021), with a short main shock rupture duration and high stress drop (Supendi *et al.* 2021).

The Mamuju earthquake struck the western coast of Sulawesi in the regions between Mamuju and Majene on an early Friday morning (Fig. 1). According to Indonesia's National Search and Rescue Agency, the event resulted in over 100 casualties (Merdeka 2021a), with over 7800 houses damaged (BNPB 2021), and no less than 37 000 people displaced (Merdeka 2021b). Previous work by Supendi *et al.* (2021), who relocated foreshocks and aftershocks recorded between the 2021 January 14 and 20, suggest that the causative fault of the Mamuju earthquake is the MSTM (Supendi *et al.* 2021, Fig. 1). This earthquake raises questions regarding seismic hazard in the Mamaju and Majene regions which remain poorly understood.

In this study, we use seismic observations and Global Positioning System (GPS) data to investigate the source of the earthquake rupture. First, we use teleseismic data to estimate the main shock's focal mechanism and coseismic slip distribution. We then relocate several new aftershocks that were not included in previous studies. Second, we determine the fault plane that ruptured during the main shock event by comparing teleseismic-based synthetic displacements with our GPS data. We perform a nonlinear inversion using our GPS data to obtain further evidence identifying the ruptured fault plane. Third, in addition to studying the underlying faulting mechanism, we create a damage proxy map (DPM) using Sentinel-1 Synthetic Aperture Radar (SAR) scenes, which allows us to evaluate the effect of the main shock on damaged buildings. Fourth, we analyse the effect of Coulomb stress changes induced by the main shock on the along-depth distribution of aftershocks. Lastly, we perform strain rate analysis using interseismic GPS velocities to evaluate the seismic hazard potential in the Mamuju and Majene regions.

2 DATA ANALYSIS, MODELLING STRATEGY AND DAMAGE PROXY MAP

2.1 Moment tensor inversion

We performed broad-band waveform modelling of teleseismic data to determine the focal mechanism and depth of the earthquake (Fig. 2). Conducting our own modelling, rather than using solutions provided by routine catalogues, allows us to explore how well resolved the solution is and to overcome trade-offs between event parameters that exist for long-period inversions such as the Global Centroid Moment Tensor (GCMT) catalogue (Tsai *et al.* 2011). We conducted waveform inversions at higher frequencies (Fig. 2b) than the GCMT catalogue (Ekstrom *et al.* 2012), which should allow better resolution of fault geometry and centroid depth.

We downloaded available teleseismic waveforms from the Incorporated Research Institutions for Seismology (IRIS) Data Management Centre (Figs 2b and c) and removed stations with a low signal-to-noise ratio or with complex waveforms that cannot be modelled with a global 1-D velocity model. We used extended *P* and *SH* waves with 90 s windows containing the direct and depth phases (Fig. 2b). These phases travel near-vertically through the crust and so are less sensitive to complex crustal velocity variations. We used the Cut-and-Paste (CAP) method to invert these waveforms to find the best-fitting double couple focal mechanism and centroid depth (Zhu & Helmberger 1996). The best-fitting source parameter was determined to give the highest cross-correlation coefficient between synthetic and real waveforms. Waveforms were shifted independently to maximize the cross-correlation coefficient, to account for velocity variations from the 1-D global model used (IASP91, Kennett & Engdahl 1991). We ran the inversions using a range of source durations to find the best-fitting depth (Fig. 2d). The results for the focal mechanism and depth of the earthquake are shown in Fig. 2 and Table S1 (Supporting Information).

2.2 Earthquake relocation

The regional seismic network of Indonesia's Meteorological, Climatological, and Geophysical Agency (BMKG, Fig. S1, Supporting Information) recorded seven foreshocks of magnitude 2.8 to 5.9—the largest earthquake during the 12 hr prior to the main shock. The network recorded 27 aftershocks of magnitude 2.4–4.9 up until 2021 July 15. In this study, we combined the relocated events from Supendi *et al.* (2021), during the period 2021 January 14–20, with four new events of magnitude 2.5 to 3.8 from 2021 January 20 to July 15. All new aftershocks were relocated using the same procedures employed in Supendi *et al.* (2021)—more details about the relocation procedure can be found in Supendi *et al.* (2021). The relocation results are shown in Fig. 3.

2.3 GPS processing

According to an empirical formula that approximates the radius of influence of an earthquake (Herring *et al.* 2016), coseismic offsets of more than 1 mm will be detected by GPS stations within ∼107 km from the main shock's epicentre. Therefore, we processed the daily recordings (from 2020 December 14 to 2021 February 14) of three GPS stations from Indonesia's Geospatial Information Agency (BIG) that are within the radius of influence (Fig. S2, Supporting Information). We processed the BIG GPS data using the GPS at MIT (GAMIT)/Global Kalman filter software packages version 10.71 (Herring *et al.* 2018). The GAMIT software employs double-differencing techniques to estimate station positions, atmospheric delays, satellite orbits and earth orientation parameters from ionosphere-free linear combination GPS phase observations. During the GAMIT processing, we fixed the satellite orbit parameters to the International GNSS Services (IGS) final orbit. In addition, we included 12 IGS stations (ALIC, COCO, DARW, DGAR, GUAM, HYDE, IISC, LHAZ, PIMO, PNGM, XMIS and YARR) to obtain the loosely constrained positions of GPS stations. Then, we combined our solution with the global GPS solution developed by the MIT analysis centre. In this step, we mapped the loosely constrained solution into a well-constrained reference frame by minimizing the position and velocity differences of selected sites with respect to *a priori* values defined by the realization of the International Terrestrial Reference Frame 2014 (ITRF2014, Altamimi *et al.* 2016). Finally, we examined the position time-series to estimate the coseismic offsets following the method of Feng *et al.* (2015, Figs S3–S5, Supporting Information). Since the M_W 5.9 foreshock event occurred on the same day as the main shock event, it is not possible to isolate the main shock offset because high-rate (1 s sampling) data are not available. Thus, our coseismic offsets (Table S2, Supporting Information) include surface displacements due to both the foreshock and main shock events.

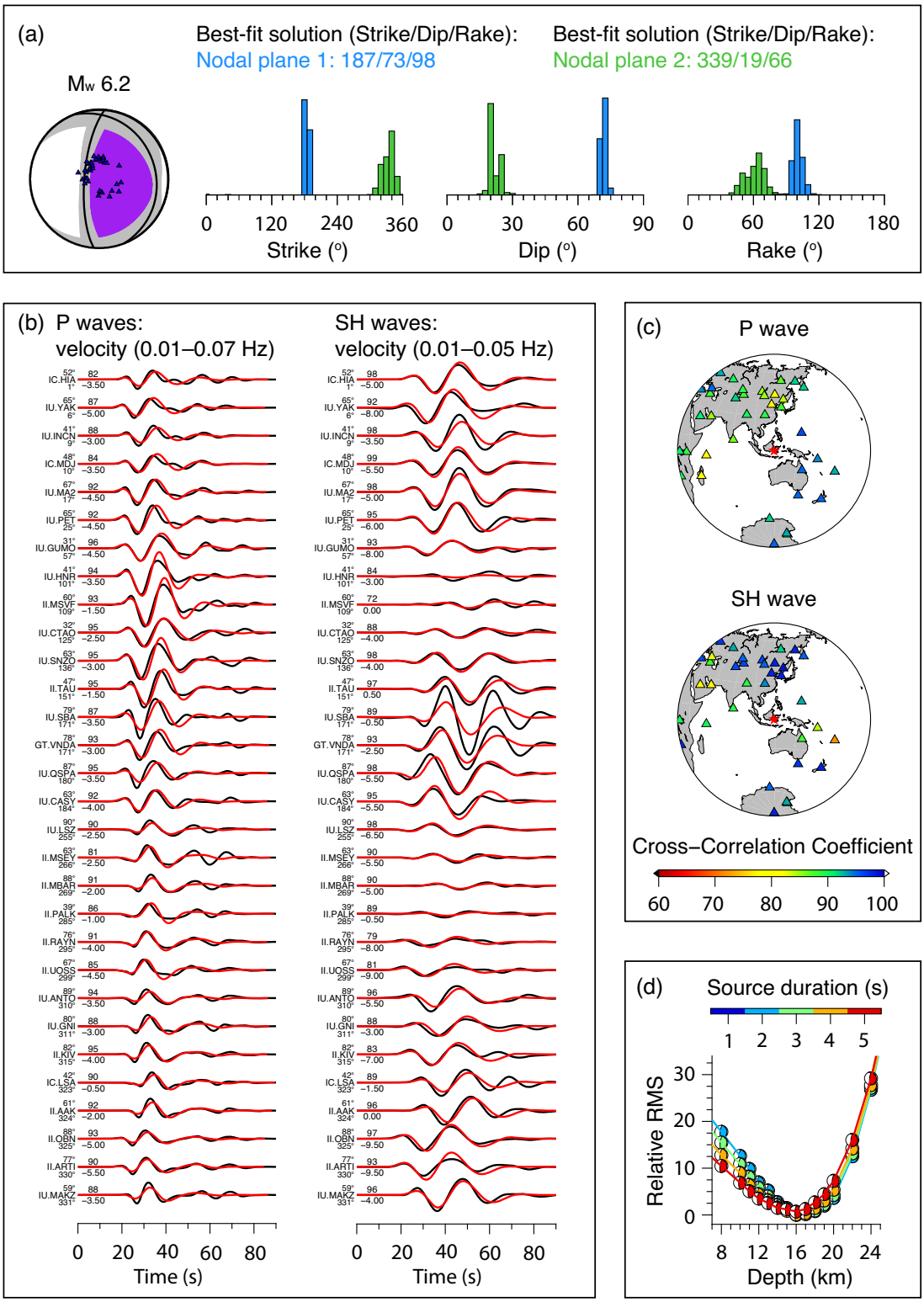

Figure 2. CAP inversion results for the M_W 6.2 main shock event. (a) Moment tensor solution for the two nodal planes of the main shock event. (b) Waveform fits. (c) Distribution of teleseismic stations used and the cross-correlation coefficients for *P* and *SH* waves. (d) Best-fitting depth (16 km) based on the rms value, and for different source duration.

2.4 Modelling earthquake source

We conducted kinematic slip inversion modelling of teleseismic body waves to estimate the slip distribution of the main shock (Kikuchi & Kanamori 1982, 1991, 2003). We avoid jointly inverting teleseismic and geodetic data for two reasons: (1) the GPS coseismic offsets are contaminated by surface displacements of the M_W 5.9 foreshock and (2) interferograms based on the available *C*-band Sentinel-1 scenes (2021 January 10 and 22) and *L*-band ALOS-2

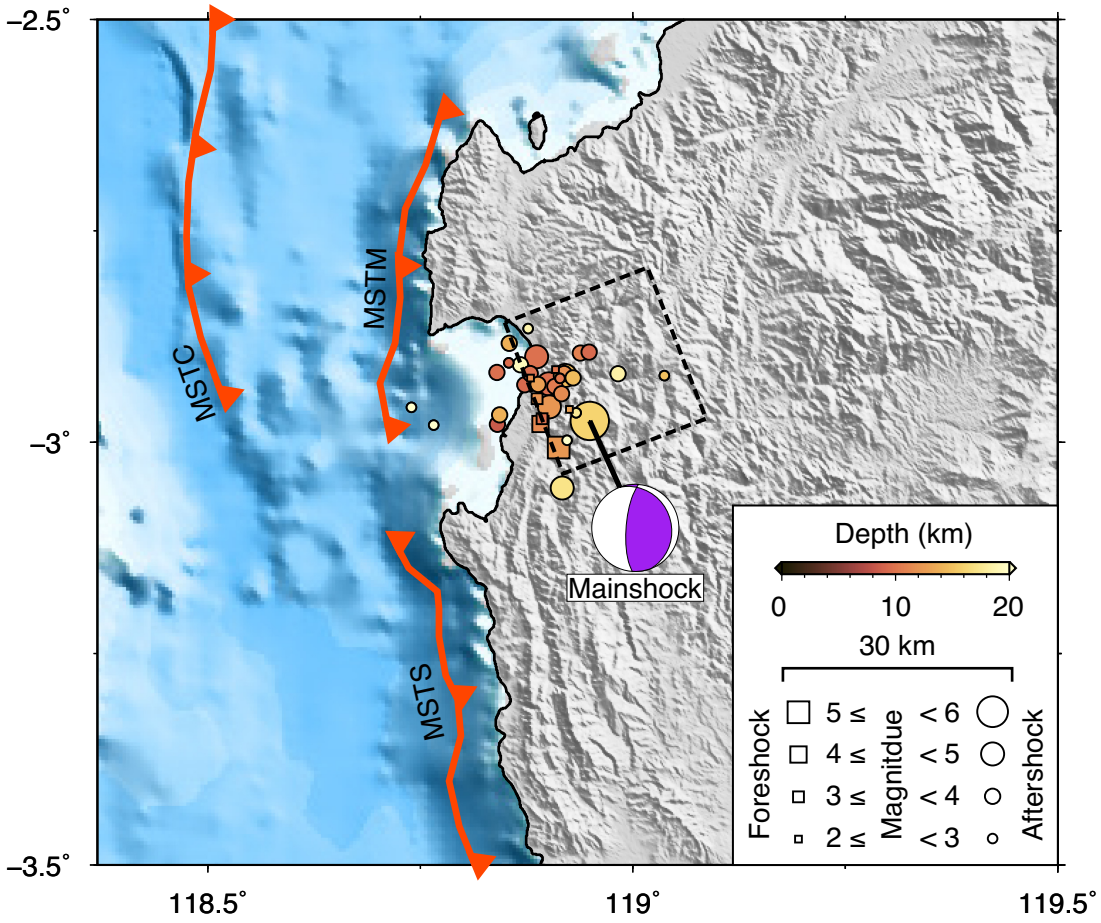

Figure 3. Relocation results for the foreshock, main shock and aftershock events. The dashed line represents the preferred main shock fault plane in the subsurface, dipping to the east.

scenes (stripmap imaging mode, 2020 April 14 and 2021 January 19), processed using modules of the InSAR Scientific Computing Environment (Rosen *et al.* 2012; Liang & Fielding 2017), do not show obvious coseismic surface displacements (Fig. S6, Supporting Information). In the teleseismic slip inversion, we used broad-band seismograms within the distance range of 28°–90° downloaded from the IRIS Data Management Centre. We used 43 *P* waves on the vertical component and 13 *SH* waves on the transverse component with a time window of 40 s. The instrument response was deconvolved to obtain displacement waveforms, which were then bandpass filtered between 2 and 200 s (or 0.005 and 0.5 Hz) for *P* waves, 5 and 200 s (or 0.005 and 0.2 Hz) for *SH* waves. The higher frequency filter ranges were adopted to resolve the details of the earthquake slip distribution. We computed Green's functions using the 1-D velocity model derived from the Crust1.0 model (Laske *et al.* 2013) for the source region and the 1-D IASP91 velocity model (Kennett & Engdahl 1991) for areas outside the source region. We set a slightly larger fault area (21 × 21 km) than that based on the Wells & Coppersmith (1994) magnitude to rupture area relationship, to accommodate the complexity of the coseismic slip distribution. Then, we divided the fault area into 3 × 3 km grids and fixed the strike and dip angle of the fault to our moment tensor solution (Fig. 2a). We allowed the rake to vary within ± 45°. We tested the two fault planes obtained from our moment tensor solution (Fig. 2a). Since the rupture velocity (*Vr*) influences the slip model significantly, we tested various *Vr* values from 1 to 4.5 km s^{-1}. We also varied the hypocentre location, and found that the best waveform fits were obtained for a hypocentre at 15 km depth. The coseismic slip modelling results are shown in Figs 4 and 5.

To further identify the fault plane that ruptured during the main shock, we used the GPS coseismic offsets in two approaches. First, we performed forward modelling using the obtained teleseismic slip models to produce synthetic displacements at the GPS stations, and then compared the synthetic displacements with the observed GPS offsets. Second, we conducted a nonlinear grid-search inversion using the GPS offsets. In these approaches, we computed Green's functions using dislocation models in an elastic half-space (Okada 1985).

We compared observed data with modelled synthetic data using a misfit function defined as:

$$X^2 = (\mathbf{d} - \mathbf{G}(\mathrm{m}))^T \mathbf{C}_d^{-1} (\mathbf{d} - \mathbf{G}(m)) \quad (1)$$

where **d** corresponds to GPS offsets, **G** to the Green's functions, **m** to the free parameters of the fault and $\mathbf{C}_\mathrm{d}$ to the covariance matrix of the GPS offsets. In the grid-search nonlinear inversion, we assumed uniform slip on a rectangular fault, and searched only for the rectangular fault's location (longitude, latitude and depth associated with the upper left corner of the rectangular fault). We fixed the slip rake, the strike and dip of the rectangular fault to our moment tensor solution (Fig. 2a). We also fixed the length and width of the rectangular fault and prescribed a uniform slip based on empirical relationships for a typical thrust earthquake of M_W 6.2

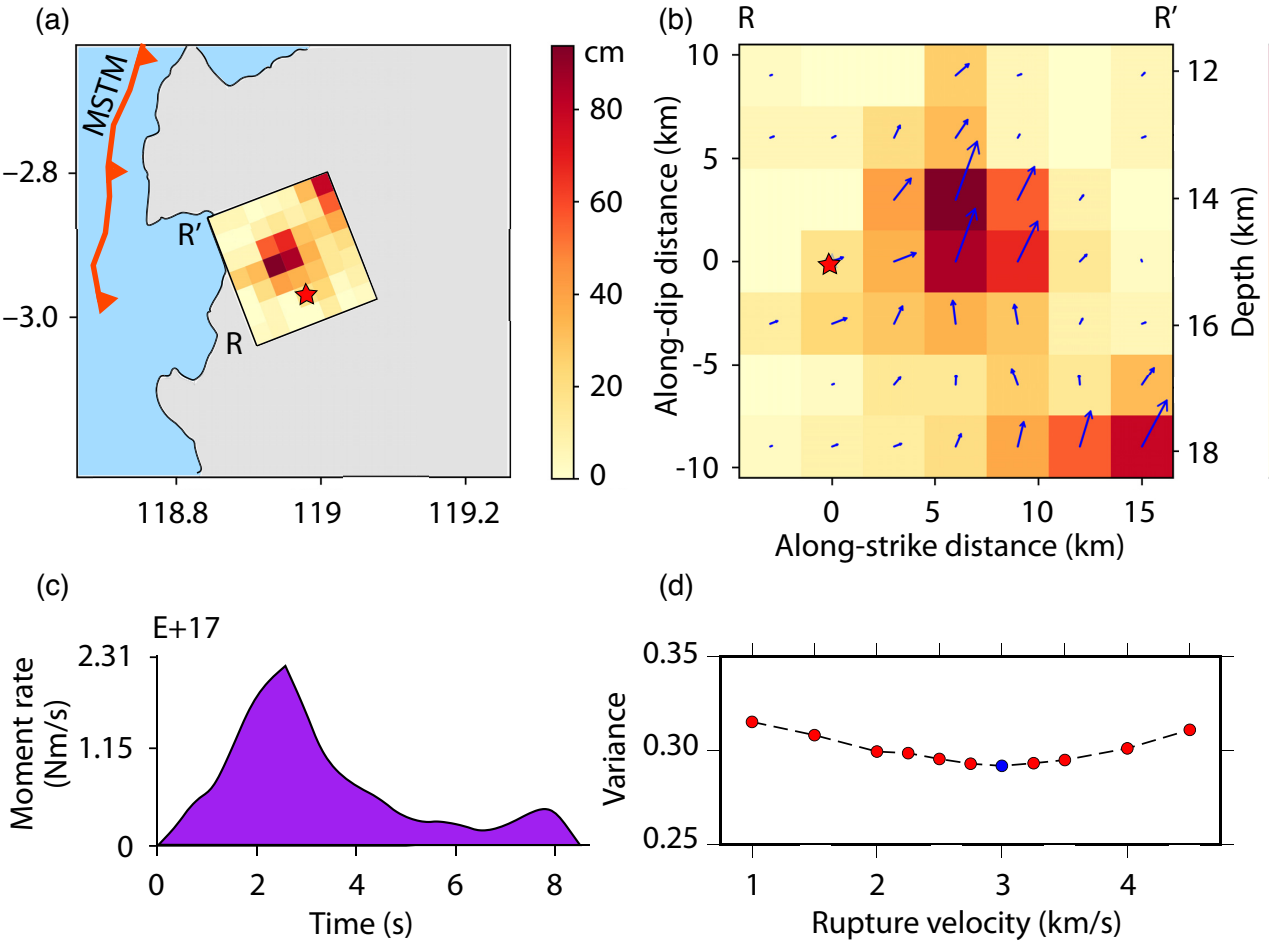

Figure 4. Preferred teleseismic slip inversion results based on the east-dipping fault. (a) and (b) Coseismic slip distribution with a maximum slip of ∼90 cm at a depth of 14 km. The red star is the hypocentre location, and the blue arrows represent the rake angle in each grid. (c) A moment-rate function for the coseismic slip distribution. (d) A variety of rupture velocities tested for the slip inversion. The preferred rupture velocity (3.0 km s^{-1}) is marked as a blue circle.

(Wells & Coppersmith 1994). Additionally, while we specified a 50-km grid-search range from the epicentre location in the west, south and east directions, we restricted the northern limit of the grid search to the distribution of the relocated foreshocks and aftershocks. We applied this constraint to avoid bias in the inversion result, which will locate the rectangular fault towards the CMJU GPS station since it is the only station that recorded significant offset. The forward and inversion modelling results are shown in Fig. 6.

2.5 Damage proxy map

We derived a DPM (Yun *et al.* 2015; Jung *et al.* 2017) from 12 Copernicus Sentinel-1 SAR interferometric coherence images acquired between 2020 November 23 and 2021 January 16, to evaluate the effect of the Mamuju earthquake on damaged buildings. To obtain the DPM, we used the method of Jung *et al.* (2017), which removes decorrelation effects that contaminate the coherence signals after a destructive disaster such as an earthquake. The method calculates probability density functions of the historical change of each SAR pixel and constructs a map of damage probability due to the earthquakes. The resulting DPM contains pixels associated with damage scaled by damage probability from 0.9 to 1, where a higher damage probability corresponds to more severe damage, such as completely collapsed buildings (Fig. 7). False alarms may be present over vegetation where coherence changes may be random.

3 RESULTS

Our moment tensor solution shows that the main shock event ruptured either a steep west-dipping fault plane or a shallow east-dipping fault plane (Fig. 2a). The event could be generated by the steep west-dipping fault plane related to the north–south surface geomorphic expressions in the epicentre location (Fig. 3). However, comparison between the strike of the east-dipping fault plane and the spatial distribution of the relocated events, suggests that the east-dipping fault plane is the more likely (Fig. 3). Determining the ruptured fault plane based on our teleseismic modelling results is inconclusive. Both the east- and west-dipping fault planes fit the waveform data equally well and result in a similar variance: 2.82 for the east-dipping fault and 2.81 for the west-dipping fault (Figs 4 and 5, Figs S7 and S8, Supporting Information). These similar results are not surprising given the main shock magnitude, the use of teleseismic data and the faulting style (waveforms generated by thrust earthquakes are not as unique as those caused by strike-slip earthquakes).

Nevertheless, our forward and inverse GPS modelling results indicate that the main shock event ruptured the east-dipping fault

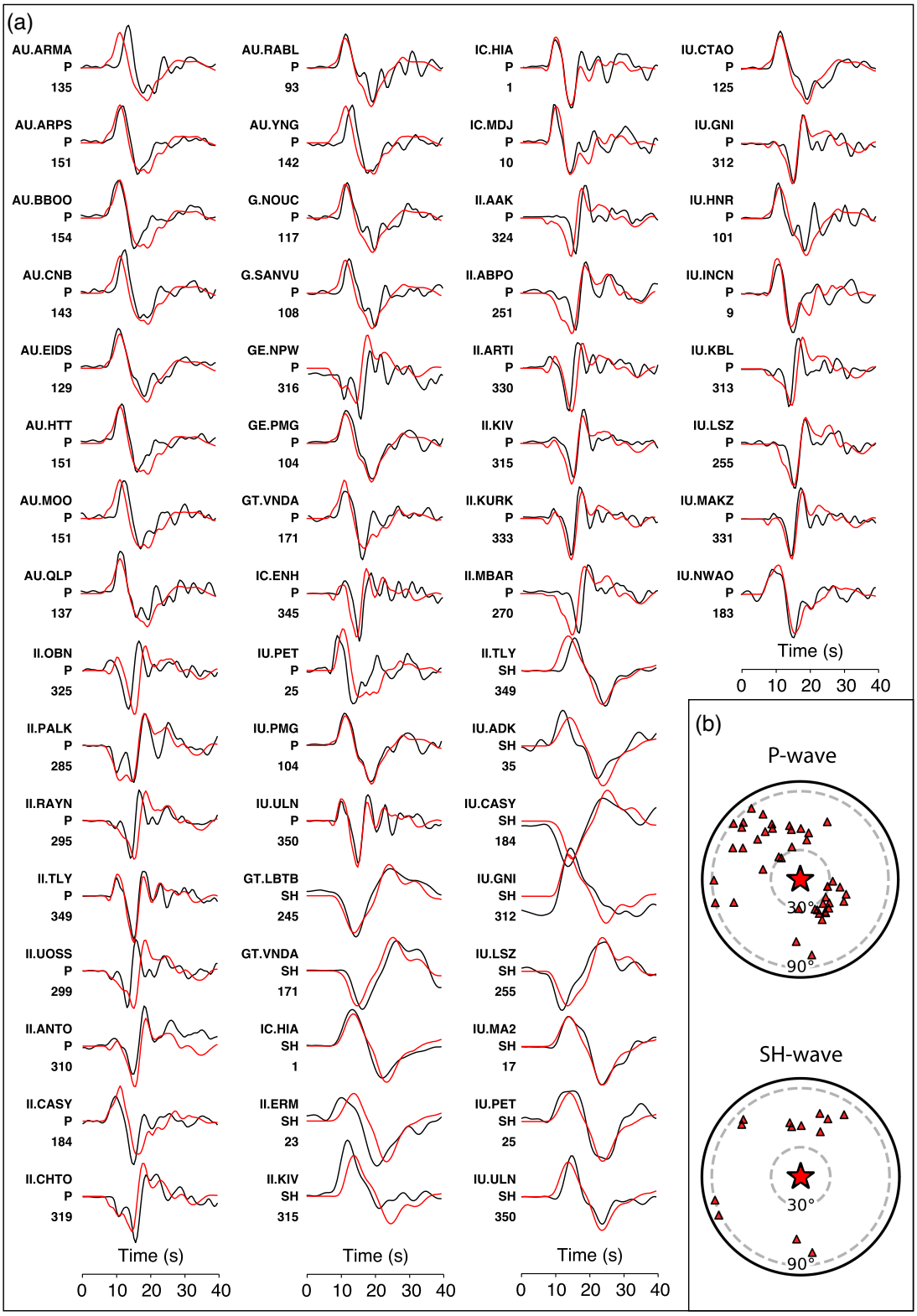

Figure 5. (a) Teleseismic waveform fits based on the preferred coseismic slip model. Data (black) and synthetic (red) waveforms are filtered to 0.5 Hz for *P* wave and to 0.2 Hz for *SH* wave. Each waveform is labelled with the station code, type of seismic wave and station azimuth. (b) Station distribution for *P*- and *SH*-wave data used in the inversion.

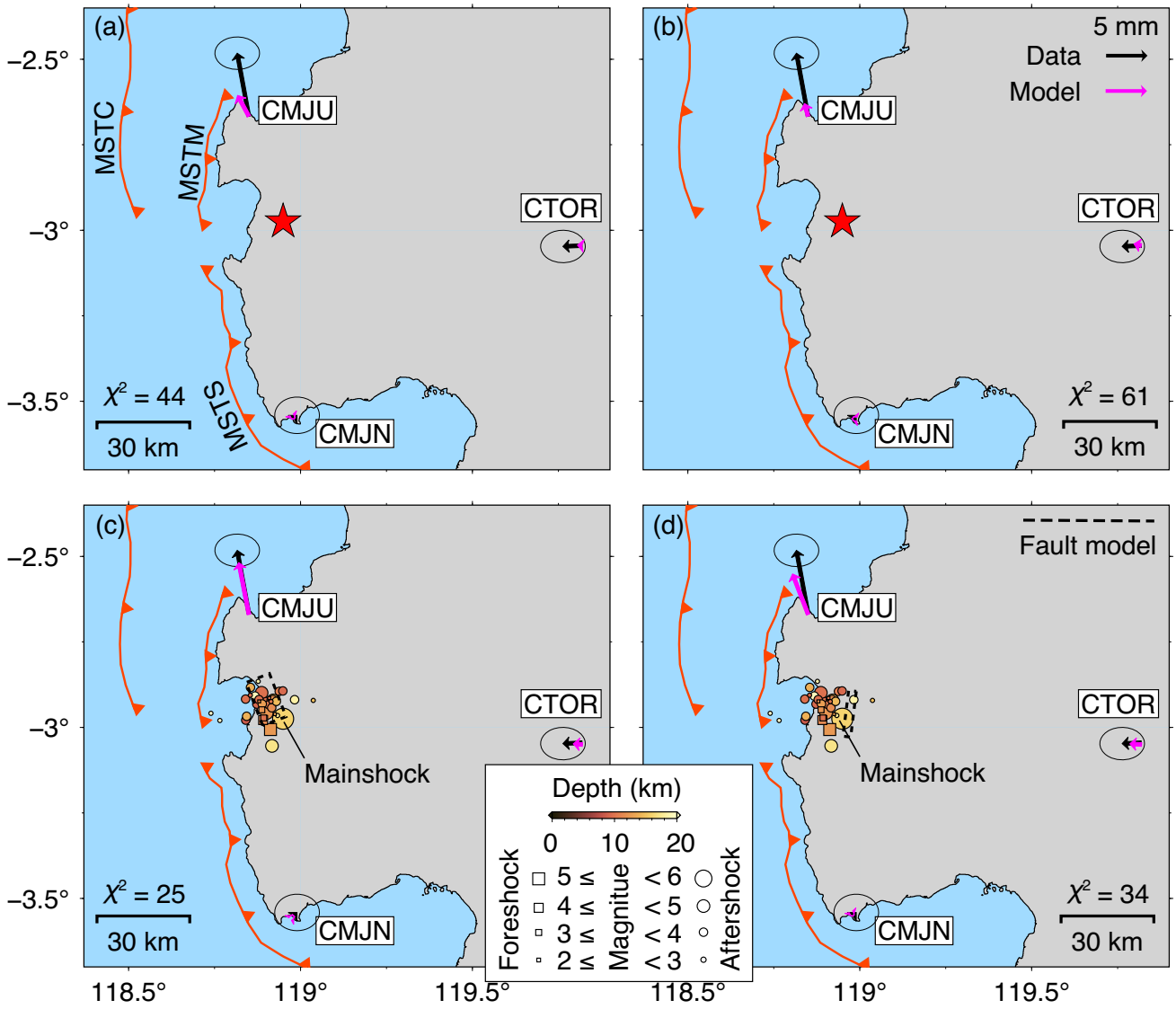

Figure 6. Forward and inverse modelling results indicate that the main shock ruptured the east-dipping fault plane. (a) and (b) Comparison of GPS offsets and teleseismic-based synthetic displacements generated using the east-dipping fault (a) and the west- dipping fault (b). The east-dipping fault results in synthetic displacements with a better fit to the GPS offsets ($X^2 = 44$) compared to that based on the west-dipping fault ($X^2 = 61$). We note that the synthetic displacement at the CMJU GPS (a) is far smaller than the observed offset. We attribute the misfit to the fact that the synthetic displacements are based on only the teleseismic slip of the main shock event. In contrast, the GPS offsets include surface displacements due to both the M_W 5.9 foreshock and M_W 6.2 main shock events. (c) and (d) Nonlinear grid-search inversion results based on the east-dipping fault (c) and the west-dipping fault (d). The east-dipping fault results in synthetic displacements with a better fit to the GPS offsets ($X^2 = 25$) compared to that based on the west-dipping fault ($X^2 = 34$).

plane, explained as follows. Forward modelling shows that the synthetic displacement based on the teleseismic slip using the east-dipping fault better fits the coseismic offset at the CMJU GPS station ($X^2 = 44$) than that based on the west-dipping fault ($X^2 = 61$, Figs 6a and b). We notice that the synthetic displacement at the CMJU GPS station (Fig. 6a) is far smaller than the observed offset. We attribute the large misfit to the fact that the synthetic displacement is based on only the slip model for the main shock event, whereas the GPS offsets include surface displacements due to both the M_W 5.9 foreshock and M_W 6.2 main shock. In addition to the forward modelling results, our nonlinear inversion results show that the east-dipping fault plane produces synthetic displacements with a better fit to the coseismic offset at the CMJU GPS station ($X^2 = 25$) than that based on the west-dipping fault plane ($X^2 = 34$, Figs 6c and d, Figs S9 and S10, Supporting Information). Taken together, these results from forward and inverse modelling of GPS data, as well as relocated aftershocks, suggest that the main shock ruptured the east-dipping fault plane.

Our preferred coseismic slip model, shows that the main shock has a maximum slip of ∼90 cm at a depth of 14 km (Fig. 4). Assuming a shear modulus of 32 GPa around the fault, our preferred coseismic slip is equivalent to M_W 6.29. In addition to the main shock's source characteristics, our DPMs show that the Mamuju region ∼30 km from the epicentre location experienced more damaged buildings than the Majene and south Mamuju regions ∼10–15 km from the epicentre location (Fig. 7). Besides the difference

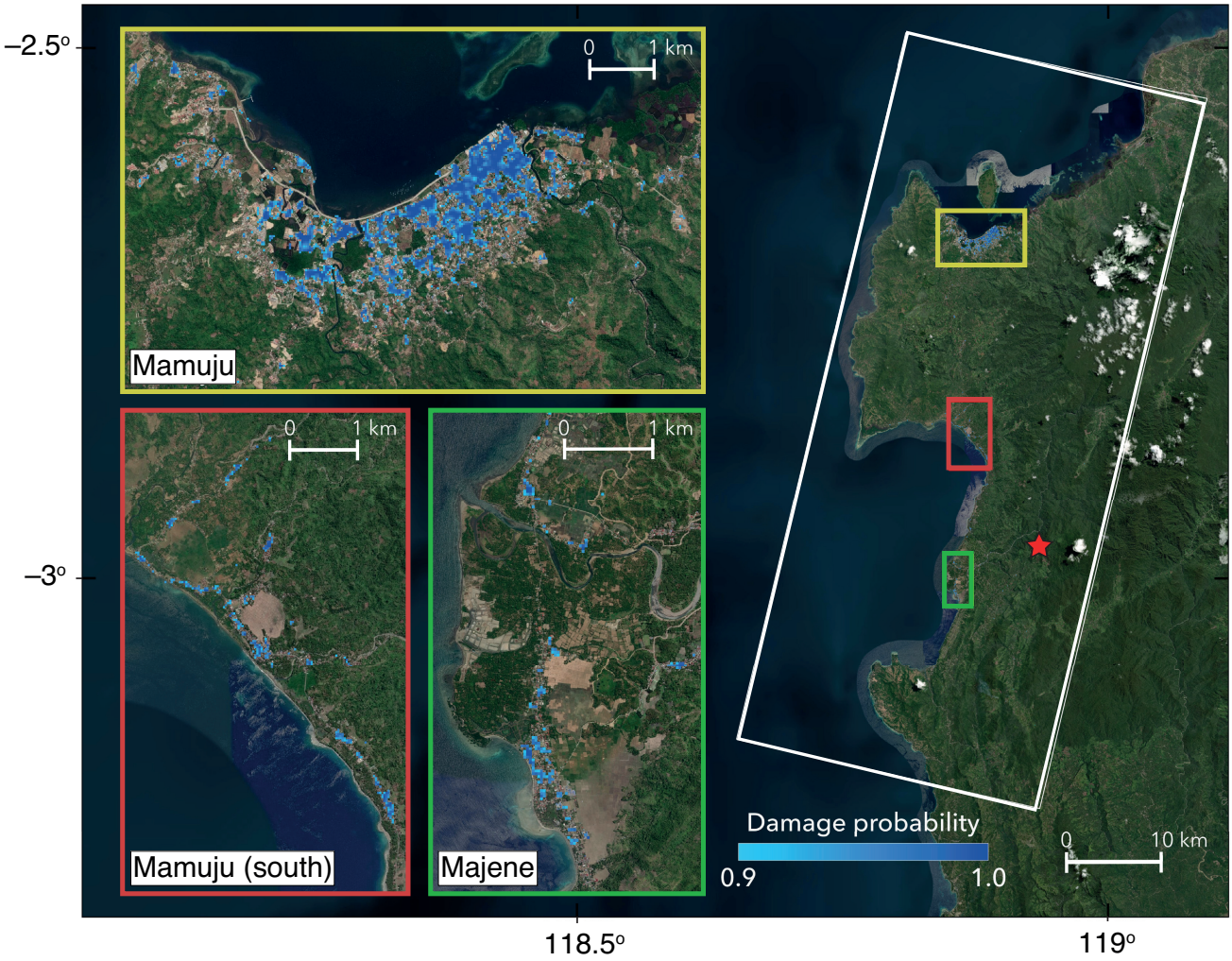

Figure 7. A DPM shows that the Mamuju region ∼30 km from the epicentre location of the Mamuju earthquake (red star) experienced more building damage than the south Mamuju and Majene regions ∼10–15 from the epicentre location. Light to dark blue pixels show increasingly significant levels of damage due the earthquake. The white polygon indicates the map extent.

in population density, both regions may have experienced different seismic ground motions due to the difference in sediment thickness, thus leading to distinct impacts on buildings.

4 DISCUSSION

Our interpretation of the east–west profile of the fault plane, combined with focal mechanisms of the 1969 Majene and 2021 Mamuju earthquakes and insights from regional cross-sections through the MST (Calvert & Hall 2007; Morley *et al.* 2011), suggests that the Mamuju earthquake ruptured a fault associated with the MSTM (Fig. 8). Additionally, we find that coseismic slip mainly occurred at depths greater than 12 km (Fig. 4b) and did not rupture the shallow section of the MSTM (Fig. 8), indicating that the Mamuju event partially ruptured the MSTM. This partial-rupture behaviour is similar to the mid-crustal ruptures observed during the 2018 Lombok earthquake sequence, in which two M_W 6.9 thrust earthquakes ruptured a shallow-dipping (25°) mid-crustal seismogenic zone, but the ruptures did not propagate to the shallow crustal levels of the Flores Thrust (Salman *et al.* 2020; Supendi *et al.* 2020; Lythgoe *et al.* 2021). The structural setting of the Lombok and Mamuju earthquakes is notably similar; in both cases, the earthquakes are located near the end of a larger fault system where the total slip of the ramp thrust fault is relatively low, the ruptured ramp fault transitions upward into a shallowly dipping décollement overlain by thick sediments, and the lower plate consists of previously thinned continental crust along the margin of an incoming continental platform. This specific geological situation may create the necessary conditions for dominantly mid-crustal thrust faulting, where only the largest ruptures involve coseismic slip of the upper ramp and shallow décollement faults.

Another striking result is that most of the aftershocks align along a plane that dips ∼40°, suggesting the activation of a secondary fault structure above the main shock fault plane (Fig. 8). We evaluate the effect of stress changes induced by the main shock event on the along-depth distribution of the aftershock events. For this purpose, we use our preferred coseismic slip distribution to calculate static Coulomb stress changes for optimal thrust faults using the Coulomb software package version 3.3 (Lin & Stein 2004; Toda *et al.* 2005) and a friction coefficient of 0.8 for thrust events (Parsons *et al.* 1999). Then, we plot the result along a vertical profile from C to D (Fig. 8). The result shows that most of the aftershocks dipping in a ∼40° plane correlate with more than 10 kPa

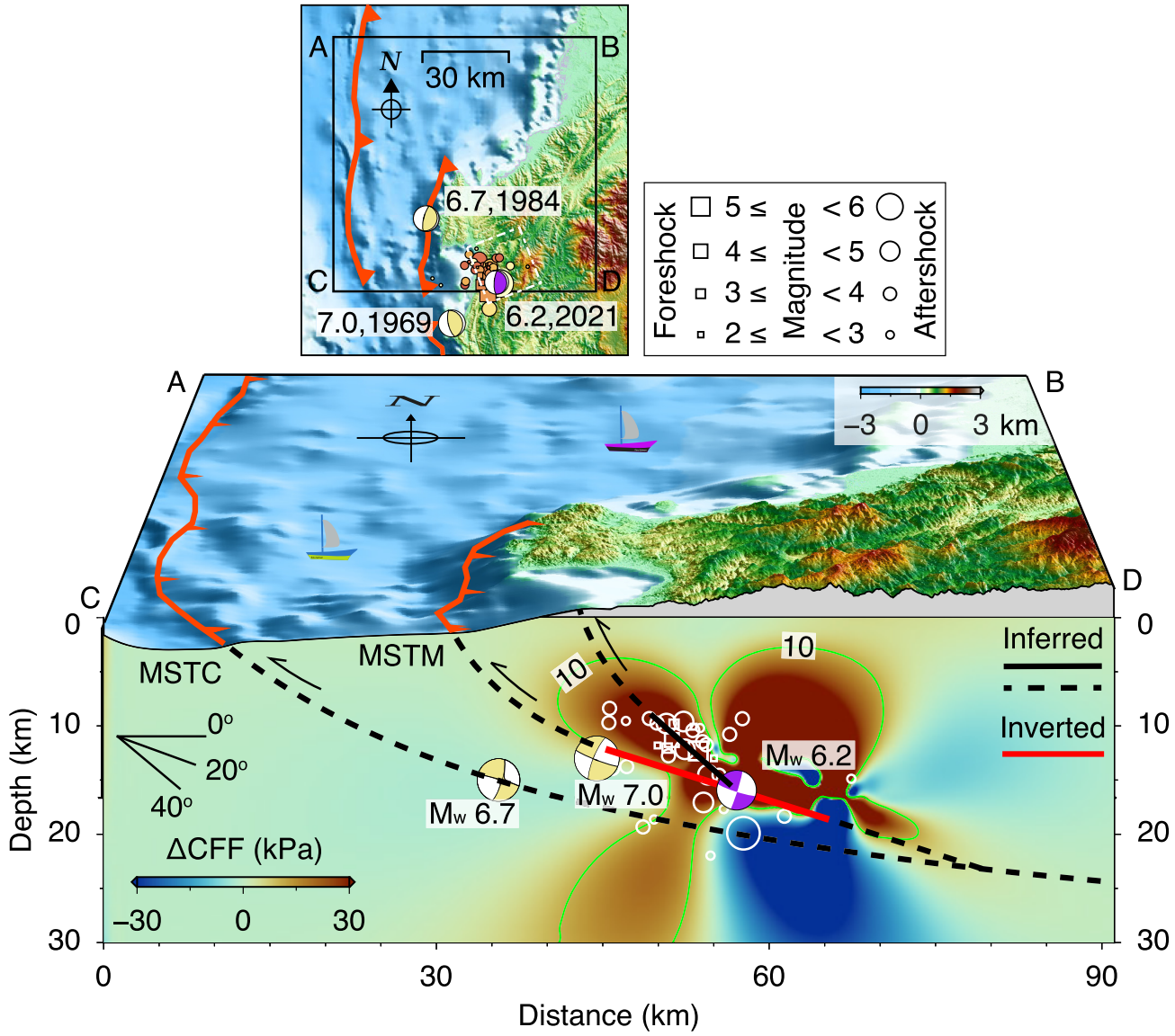

Figure 8. A schematic profile of the Makassar Strait Thrust in West Sulawesi beneath the Mamuju and Majene regions based on the modelling results, relocation results, moment tensor solution for the Mamuju event, focal mechanisms of the 1969 and 1984 events, combined with insights from a regional cross-section through the MST (Calvert & Hall 2007; Morley *et al.* 2011). Different from the dipping angle of the main shock fault plane (19°, red line), most of the relocated aftershocks form a plane that dips at an angle of ∼40° (solid black line), indicating the existence of a secondary fault structure. The ∼40°-dipping secondary fault and the updip sections of the MSTM overlap with areas of more than 10 kPa positive Coulomb stress change (background colour). The MSTM, the MSTC and the possible secondary fault form a series of imbricate thrust faults in West Sulawesi beneath the Mamuju and Majene regions.

positive Coulomb stress changes (Fig. 8), which is above the typical earthquake triggering threshold (King *et al.* 1994; Hardebeck *et al.* 1998). To check whether a positive correlation exists between the large Coulomb stress changes (≥10 kPa) and location of aftershock events dipping in a ∼40° plane, we calculated the Coulomb stress changes due to the main shock event (source) at the location of the 40°-dipping thrust fault (receiver). Our calculation shows that only ∼50 per cent of the aftershock events are within ≥ 10 kPa Coulomb stress changes (Fig. S11, Supporting Information). The remaining aftershock events are within the negative Coulomb stress change area. This result suggests that coseismic Coulomb stress changes alone were not responsible for promoting all the aftershock events. However, the main shock was likely to have been followed by afterslip, which may have imparted cumulative positive Coulomb stress changes on the 40°-dipping thrust fault, thus promoting the occurrence of the aftershock events (e.g. Chan & Stein 2009; Jiang *et al.* 2021). Our calculation of the Coulomb stress changes suggests two implications. First, the positive stress changes induced by the main shock event promoted the activation of a secondary fault structure. Second, the updip unruptured sections of the MSTM were likely brought closer to failure due to the induced positive stress changes (Fig. 8) and will potentially become the source of future earthquakes. Taken together, the MSTM, the MSTC and the possible reactivated secondary fault form a series of imbricate thrust faults in West Sulawesi beneath the Mamuju and Majene regions (Fig. 8).

We assess the seismic hazard in the Mamuju and Majene regions by deriving the principal strain and second invariant rates from interseismic GPS velocities spanning 1998–2004 (Simons *et al.* 2007)

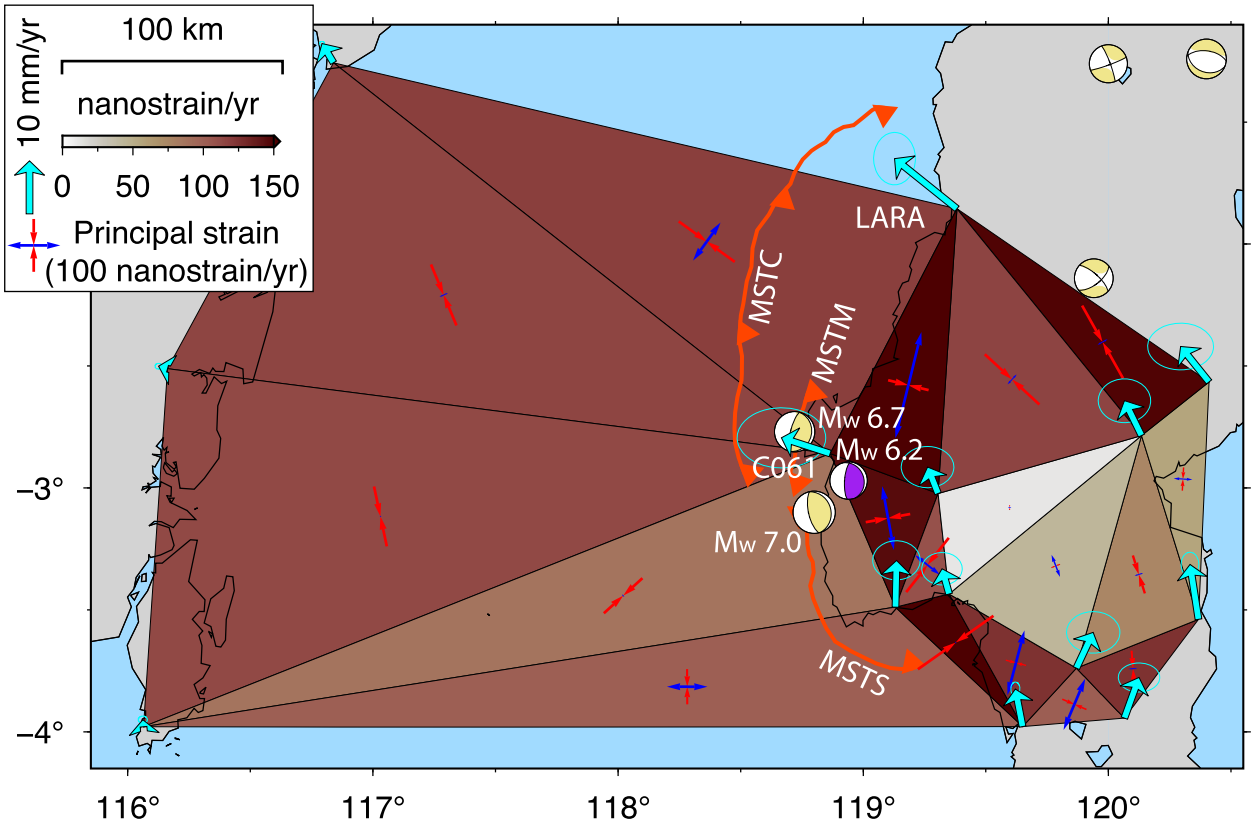

Figure 9. Second invariant (coloured triangles) of the principal strain-rate tensors, derived from interseismic GPS velocities (cyan vectors) relative to the Sunda reference frame (Yong *et al.* 2017). The inward red arrows represent compression of the principal strain rate, while the outward blue arrows represent extension. Focal mechanisms are associated with the Mamuju 2021 earthquake and all instrumentally recorded $M_W > 6$ earthquakes (Fitch 1972; GCMT catalogue).

and 2010–2015 (Susilo *et al.* 2016; Table S3, Supporting Information). We computed the strain tensors within elements of a triangular network that connects each of our GPS stations (McCaffrey *et al.* 2000; Bock *et al.* 2003). Then, we estimated the principal strain and second invariant rates in each triangular mesh. The results show that principal strain patterns describe compression in the Mamuju and Majene regions (Fig. 9). Additionally, our results indicate that the second invariant rates are higher along the western coastline of the Mamuju and Majene regions than in the surrounding areas to the east (Fig. 9, see also Fig. S12, Supporting Information). This result, combined with the fact that the region produced three $M_W > 6$ earthquakes over the last 100 yr, implies that the MSTC, the MSTM and the MSTS pose substantial seismic hazard to population centres along the western coastline of the Mamuju and Majene regions.

The updip unruptured section of the MSTM could produce future earthquakes similar to or larger than the magnitude of the 2021 Mamuju earthquake. Future larger earthquakes may potentially generate secondary hazards to coastal communities both along the western coast of Sulawesi and the eastern coast of Borneo (Fig. 1), such as submarine landslide-triggered tsunamis (hereafter referred to as 'SLTTs'). The SLTTs are possible to occur due to the existence of numerous steep slope areas on the seafloor of the Makassar Strait (Brackenridge *et al.* 2020), which could be destabilized by the seismic shaking of earthquakes (Ten Brink *et al.* 2014). For example, Brackenridge *et al.* (2020) have identified 16 submarine landslide scars in the seafloor of the Makassar Strait that correlate with locations of steep submarine slopes. Nugraha *et al.* (2020) also identified one submarine landslide scar, known as the Haya slide, located ∼30 km to the west of the epicentre location of the 1969 M_W 7.0 earthquake (Fig. 1).

The 1969 event was followed by a moderate tsunami (Soloviev & Go 1974) that killed 64 people (Prasetya *et al.* 2001). However, tsunami simulations by Pranantyo *et al.* (2022) failed to reproduce the highest 4-m tsunami height (Soloviev & Go 1974) if only considering seafloor displacements due to the main shock slip of the 1969 event. Their study suggests that the 4-m tsunami height could be explained by a local submarine landslide induced by the 1969 main shock event. Therefore, although the actual age of the Haya slide has not yet been confirmed, the proximity of the Haya slide to the tsunami which followed the 1969 event, indicates the Haya slide is a candidate for triggering the 1969 tsunami.

The threat of SLTTs has been further highlighted by Pranantyo *et al.* (2021) based on tsunami modelling using two different scenarios of submarine landslides on the Makassar Strait. The first tsunami modelling scenario using a 5-km^3-submarine landslide (Brackenridge *et al.* 2020) generates ∼2.9 and ∼1.1 m maximum tsunami amplitudes on the western coast of Sulawesi and the eastern coast of Borneo, respectively. The second tsunami scenario using a 225-km^3-submarine landslide (Brackenridge *et al.* 2020) generates ∼11 and ∼4.3 m maximum tsunami amplitudes on the western coast of Sulawesi and the eastern coast of Borneo, respectively.

The plan by Indonesia's government to move the capital city of Indonesia to East Borneo, puts this region under the spotlight,

given the expected huge increase in the population of the area. Thus, further studies are required to gain a comprehensive knowledge of the seismic hazard potential posed by the MST, including possible secondary hazards. Future work investigating the slip rate of the MST would benefit from denser GPS stations on the western coast of Sulawesi and the eastern coast of Borneo.

5 CONCLUSION

We study the 2021 January 15 M_W 6.2 earthquake that struck the Mamuju and Majene regions of West Sulawesi, Indonesia. This event caused thousands of damaged buildings within a radius of ∼30 km from the main shock' epicentre location, as shown on our DPM derived from Sentinel-1 SAR scenes. Our analysis of seismic and geodetic data indicates that the main shock event partially ruptured the east-dipping fault plane associated with the MST segment offshore west Mamuju. Comparing Coulomb stress changes induced by the main shock, with the along-depth distribution of aftershocks, suggests a possible activation of another fault structure after the main shock event. The main shock event also imparted positive Coulomb stress changes to the updip, unruptured section of the MST segment, which may become the source of future earthquakes. Our analysis of interseismic GPS velocities estimates that the Mamuju and Majene regions have a relatively higher crustal strain rate than other nearby regions. The results (partial rupture of the MST segment, the updip unruptured section of the MST segment, and high strain rate in the Mamuju and Majene regions) together suggest a significant seismic hazard potential in the Mamuju and Majene areas.

ACKNOWLEDGMENTS

We thank BMKG for providing regional seismic data and BIG for providing continuous GPS data. We are grateful to The Japanese Aerospace Exploration Agency (JAXA) for giving us ALOS-2 data access through a proposal granted to S-HY under the Third Research Announcement for Earth Observations PI no. ER3A2N085; ownership and copyright of raw data maintained by JAXA. We thank the editor Bertrand Rouet- Leduc and assistant editor Fern Storey. We are indebted to two anonymous reviewers for providing suggestions and feedback that helped improve the manuscript. The teleseismic slip inversion code is available at http://www.eri.u-tokyo.ac.jp/ETAL/KIKUCHI/. The kinematic slip models were plotted using codes from https://github.com/rokuwaki/2020Greece. Most figures were created using the Generic Mapping Tools (GMT; Wessel *et al.* 2013) and colour palettes from Crameri (2018). The relocated earthquakes from this study are available at https://zenodo.org/record/7467181#.Y-GsyexBwfv. IM is supported by RISPRO LPDP Indonesia Endowment Fund for Education S-303/LPDP.4/2022. SR is supported by the Indonesian Ministry of Research, Technology, and Higher Education through a scholarship program of 'Pendidikan Magister Menuju Doktor Untuk Sarjana Unggul (PMDSU) Batch IV (2018)'. RS, KL, KB, CT and S-HY are supported by the Earth Observatory of Singapore (EOS) via its funding from the National Research Foundation Singapore and the Singapore Ministry of Education under the Research Centres of Excellence Initiative. RS is further supported by the National Research Foundation Investigatorship Scheme (award no. NRF-NRFI05-2019-0009 to Emma Hill). This work comprises EOS contribution number 462.

DATA AVAILABILITY

Copernicus Sentinel-1 data (2018) were provided by the European Space Agency and downloaded free through the Alaska Satellite Facility (https://search.asf.alaska.edu/#/?flightDirs =). Teleseismic waveforms data are available from the Incorporated Research Institutions for Seismology (IRIS) Data Management Center (https://ds.iris.edu/ds/nodes/dmc/). We acknowledge the operators of the Australian National Seismograph Network (AU), GEOFON network (GE), GEOSCOPE network (G), Global Seismic Network (II and IU), Global Telemetered Seismic Network (GT), New China Digital Seismograph Network (IC). The Crust1.0 velocity model is available at https://igppweb.ucsd.edu/∼gabi/crust1.html. Aftershocks are available in the data repository, https://zenodo.org/record/7467181#.Y6LdlexBwfC.

CONFLICT OF INTEREST

The authors declare that they have no competing interests.

REFERENCES

Altamimi, Z., Rebischung, P., Métivier, L. & Collilieux, X., 2016. ITRF2014: a new release of the International Terrestrial Reference Frame modelling nonlinear station motions, *J. geophys. Res.: Solid Earth,* **121**(8), 6109–6131.

Badan Nasional Penanggulan Bencana (BNPB), 2021. Total Kerusakan dan Kerugian Pasca Gempa M6,2 Sulbar Capai Rp829,1 Miliar, available at https://bnpb.go.id/berita/total-kerusakan-dan-kerugian-pascagempa-m6-2-sulbar-capai-rp829-1-miliar (last accessed August 2021) (in Bahasa Indonesia).

Bergman, S. C., Coffield, D. Q., Talbot, J. P. & Garrard, R. A., 1996. Tertiary tectonic and magmatic evolution of western Sulawesi and the Makassar Strait, Indonesia: evidence for a Miocene continent-continent collision, *Geol. Soc., Lond., Spec. Publ.,* **106**(1), 391–429.

Bock, Y., Prawirodirdjo, L., Genrich, J. F., Stevens, C. W., McCaffrey, R., Subarya, C., Puntodewo, S. S. O. & Calais, E., 2003. Crustal motion in Indonesia from Global Positioning System measurements, *J. geophys. Res.*., **108**(2367), 1–21.

Brackenridge, R. E., Nicholson, U., Sapiie, B., Stow, D. & Tappin, D. R., 2020. Indonesian Throughflow as a preconditioning mechanism for submarine landslides in the Makassar Strait, *Geol. Soc. Lond. Spec. Publ.,* **500**(1), 195–217.

Calvert, S.J. & Hall, R.,2007. Cenozoic evolution of the Lariang and Karama regions, NorthMakassar Basin, western Sulawesi, Indonesia, *Petroleum Geoscience,* **13**(), 353–368.https://doi.org/10.1144/1354-079306-757

Chan, C. H. & Stein, R. S., 2009. Stress evolution following the 1999 Chi-Chi, Taiwan, earthquake: consequences for afterslip, relaxation, aftershocks and departures from Omori decay, *Geophys. J. Int.,* **177**(1), 179–192.

Crameri, F., 2018. Geodynamic diagnostics, scientific visualisation and StagLab 3.0, *Geosci. Model Develop.,* **11**(6), 2541–2562.

Di Giacomo, D., Engdahl, E.R. & Storchak, D.A., 2018. The ISC-GEM earthquake catalogue (1904–2014): status after the extension project, *Earth Syst. Sci. Data,* **10**(4), 1877–1899.

Dziewonski, A. M., Chou, T. A. & Woodhouse, J. H., 1981. Determination of earthquake source parameters from waveform data for studies of global and regional seismicity, *J. geophys. Res.,* **86**(B4), 2825–2852.

Ekström, G., Nettles, M. & Dziewoński, A. M., 2012. The global CMT project 2004–2010: centroid-moment tensors for 13,017 earthquakes, *Phys. Earth planet. Inter.,* **200,** 1–9.

Feng, L., Hill, E. M., Banerjee, P., Hermawan, I., Tsang, L. L. H., Natawidjaja, D. H., Suwargadi, B. W. & Sieh, K., 2015, A unified GPS-based earthquake catalogue for the Sumatran plate boundary between 2002 and 2013, *J. geophys. Res. Solid Earth,* **120,** 3566–3598.

Fitch, T. J., 1972. Plate convergence, transcurrent faults, and internal deformation adjacent to southeast Asia and the western Pacific, *J. geophys. Res.,* **77**(23), 4432–4460.

Gunawan, E., Kholil, M. & Widiyantoro, S., 2021 Coseismic slip distribution of the 14 January 2021 Mamuju-Majene, Sulawesi, earthquake derived from GPS data, in Springer *Natural Hazards,* pp. 1–10, https://doi.org/10.1007/s11069-021-05084-y.

Hackl, M., Malservisi, R. & Wdowinsk, S., 2009. Strain rate patterns from dense GPS networks, *Nat. Hazards Earth Syst. Sci.,* **9**(), 1177–1187, https://doi.org/10.5194/nhess-9-1177-2009.

Hall, R., 2011. Australia–SE Asia collision: plate tectonics and crustal flow, *Geol. Soc., Lond., Spec. Publ.,* **355**(1), 75–109.

Hamilton, W. B., 1979. Tectonics of the Indonesian Region, *Professional Paper 1078, USGS Numbered Series,* doi:10.3133/pp1078.

Hardebeck, J. L., Nazareth, J. J. & Hauksson, E., 1998. The static stress change triggering model: constraints from two southern California aftershock sequences, *J. geophys. Res.,* **103**(B10), 24427–24437.

Herring, T. A., King, R. W., Floyd, M. A. & McClusky, S. C., 2018. *Introduction to GAMIT/GLOBK, Release 10. 7* , Massachusetts Institute of Technology, Cambridge, Massachusetts, available at http://geoweb.mit.edu/gg/Intro_GG.pdf, (last accessed 2020 December 2020).

Herring, T. A., Melbourne, T. I., Murray, M. H., Floyd, M. A., Szeliga, W. M., King, R. W. & Wang, L., 2016. Plate Boundary Observatory and related networks: GPS data analysis methods and geodetic products, *Rev. Geophys.,* **54**(4), 759–808.

Irsyam, M. *et al.*, 2017. *Peta sumber dan bahaya gempa Indonesia tahun 2017, Cetakan pertama*. Pusat Penelitian dan Pengembangan Perumahan dan Permukiman, Badan Penelitian dan Pengembangan, Kementerian Pekerjaan Umum, Bandung. (In Bahasa Indonesia).

Jiang, J., Bock, Y. & Klein, E., 2021. Coevolving early afterslip and aftershock signatures of a San Andreas fault rupture, *Sci. Adv.,* **7**(15), 1–15.

Jung, J., Yun, S. H., Kim, D. J. & Lavalle, M., 2017. Damage-mapping algorithm based on coherence model using multitemporal polarimetric–interferometric SAR data, *IEEE Trans. Geosci. Remote Sens.,* **56**(3), 1520–1532.

Kennett, B.L.N. & Engdahl, E.R., 1991. Travel times for global earthquake location and phase association, *Geophys. J. Int.,* **105**(2), 429–465.

Kikuchi, M. & Kanamori, H., 1982. Inversion of complex body waves, *Bull. seism. Soc. Am.,* **72**(2), 491–506.

Kikuchi, M. & Kanamori, H., 1991. Inversion of complex body waves—III, *Bull. seism. Soc. Am.,* **81**(6), 2335–2350.

Kikuchi, M. & Kanamori, H., 2003. *Note on Teleseismic Body-Wave Inversion Program,* Earthquake Research Institute, Tokyo University, Tokyo, Japan, **21,** available at http://wwweic.eri.u-tokyo.ac.jp/ETAL/KIKUCHI/ (last accessed 2021 March).

King, G. C., Stein, R. S. & Lin, J., 1994. Static stress changes and the triggering of earthquakes, *Bull. seism. Soc. Am.,* **84**(3), 935–953.

Laske, G., Masters., G., Ma, Z. & Pasyanos, M., 2013. Update on CRUST1.0—a 1-degree Global Model of Earth's Crust, *Geophys. Res. Abstr.,* **15,** 2658, Abstract EGU2013-2658.

Liang, C.& Fielding, E. J.(2017) Interferometry With ALOS-2 Full-Aperture ScanSAR Data, IEEE Transactions on Geoscience and Remote Sensing, *2739,* **55,** 2739–2750, 10.1109/TGRS.2017.2653190.

Lin, J. & Stein, R. S., 2004. Stress triggering in thrust and subduction earthquakes and stress interaction between the southern San Andreas and nearby thrust and strike-slip faults, *J. geogphys. Res.: Solid Earth,* **109**(B2), doi:10.1029/2003JB002607

Lythgoe, K., Muzli, M., Bradley, K., Wang, T., Nugraha, A.D., Zulfakriza, Z., Widiyantoro, S. & Wei, S., 2021. Thermal squeezing of the seismogenic zone controlled rupture of the volcano-rooted Flores Thrust, *Sci. Adv.,* **7**(5),. doi:10.1126/sciadv.abe2348

McCaffrey, R., Zwick, P., Bock, Y., Prawirodirdjo, L., Genrich, J., Puntodewo, S. S. O. & Subarya, C., 2000. Strain partitioning during oblique plate convergence in northern Sumatra: geodetic and seismologic constraints and numerical modeling, *J. geophys. Res.,* **105**(B12), 28,363–328,376.

Merdeka, 2021a. Korban meninggal akibat gempa di Sulbar mencapai 105 orang, available at https://www.merdeka.com/peristiwa/korban-meninggal-akibat-gempa-di-sulbar-mencapai-105-orang.html (last accessed 2021 August) (in Bahasa Indonesia).

Merdeka, 2021b. 36.947 Korban Gempa Sulbar Masih di Tenda Pengungsian, available at https://www.merdeka.com/peristiwa/36947-korban-gempa-sulbar-masih-di-tenda-pengungsian.html (last accessed 2021 August) (in Bahasa Indonesia).

Morley, C.K., King, R., Hillis, R., Tingay, M. & Backe, G., 2011. Deepwater fold and thrust belt classification, tectonics, structure, and hydrocarbon prospectivity: a review, *Earth Sci. Rev.,* **104**(1-3), 41–91.

Nugraha, H. D., Jackson, C. A. L., Johnson, H. D. & Hodgson, D. M., 2020. Lateral variability in strain along a mass-transport deposit (MTD) toewall: a case study from the Makassar Strait, offshore Indonesia, *J. geol. Soc.,* **177,** 1261–1279.

Okada, Y., 1985. Surface deformation due to shear and tensile faults in a half-space, *Bulletin of the Seismological Society of America,* **75**(), 1135–1154.

Parsons, T., Stein, R. S., Simpson, R. W. & Reasenberg, P. A., 1999. Stress sensitivity of fault seismicity: a comparison between limited-offset oblique and major strike-slip faults, *J. geophys. Res.: Solid Earth,* **104**(B9), 20183–20202.

Pranantyo, I. R., *et al.* 2022. Source reconstruction of the 1969 Western Sulawesi, Indonesia, Earthquake and Tsunami, *Pure appl. Geophys.,* 1–19, 10.1007/s00024-022-03064-2.

Pranantyo, I. R., Heidarzadeh, M. & Cummins, P. R., 2021. Complex tsunami hazards in eastern Indonesia from seismic and non-seismic sources: deterministic modelling based on historical and modern data, *Geosci. Lett.,* **8**(1), 1–16.

Prasetya, G. S., De Lange, W. P. & Healy, T. R., 2001. The Makassar strait tsunamigenic region, Indonesia, *Nat. Hazards,* **24**(3), 295–307.

Puspita, S. D., Hall, R. & Elders, C. F., 2005. *Structural Styles of the Offshore West Sulawesi Fold Belt,* North Makassar straits, Indonesia.

Rosen, P. A., 2012. The InSAR scientific computing environment, *In EUSAR 2012,* **9th**(European conference on synthetic aperture radar), 730–733.

Salman, R. *et al.*, 2020. Cascading partial rupture of the Flores thrust during the 2Lombok earthquake sequence, Indonesia, *Seismol. Res. Lett.,* **91**(4), 2141–2151.

Simons, W.J.F. *et al.*, 2007. A decade of GPS in Southeast Asia: resolving Sundaland motion and boundaries, *J. geophys. Res.: Solid Earth,* **112**(B6),. doi:10.1029/2005JB003868

Socquet, A., Simons, W., Vigny, C., McCaffrey, R., Subarya, C., Sarsito, D., Ambrosius, B. & Spakman, W., 2006. Microblock rotations and fault coupling in SE Asia triple junction (Sulawesi, Indonesia) from GPS and earthquake slip vector data, *J. geophys. Res.: Solid Earth,* **111**(B8).

Soloviev, S.L. & Go, Ch. N., 1974. *A catalogue of tsunamis on the western shore of the Pacific Ocean,* Nauka Publishing House, Moscow, USSR, Canadian Translation of Fisheries and Aquatic Sciences, Canada, p. 310.

Storchak, D. A., Di Giacomo, D., Bondár, I., Engdahl, E. R., Harris, J., Lee, W. H., Villaseñor, A. & Bormann, P., 2013. Public release of the ISC–GEM global instrumental earthquake catalogue (1900–2009), *Seismol. Res. Lett.,* **84**(5), 810–815.

Storchak, D. A., Di Giacomo, D., Engdahl, E. R., Harris, J., Bondár, I., Lee, W. H., Bormann, P. & Villaseñor, A., 2015. The ISC-GEM global instrumental earthquake catalogue (1900–2009): introduction, *Phys. Earth planet. Inter.,* **239,** 48–63.

Supendi, P. *et al.*, 2020. Relocated aftershocks and background seismicity in eastern Indonesia shed light on the 2018 Lombok and Palu earthquake sequences, *Geophys. J. Int.,* **221**(3), 1845–1855.

Supendi, P. *et al.*, 2021. Foreshock–mainshock–aftershock sequence analysis of the 14 January 2(MW 6.2) Mamuju–Majene (West Sulawesi, Indonesia) earthquake, *Earth Planets Space,* **73**(1), 1–10.

Supendi, P., Nugraha, A. D., Widiyantoro, S., Abdullah, C. I., Puspito, N. T., Palgunadi, K. H., Daryono, D. & Wiyono, S. H., 2019. Hypocenter relocation of the aftershocks of the MW 7.5 Palu earthquake (September 28, 2018) and swarm earthquakes of Mamasa, Sulawesi, Indonesia, using the BMKG network data, *Geosci. Lett.,* **6**(1), 1–11.

Susilo, S., Meilano, I., Abidin, H. Z., Sapiie, B., Efendi, J. & Wijanarto, A. B., 2016. Velocity field from twenty-two years of combined GPS daily

coordinate time series analysis, in *AIP Conf. Proc.,* vol. AIP Publishing **1730**(1), p. 040003, 10.1063/1.4947393.

Ten Brink, U. S., Chaytor, J. D., Geist, E. L., Brothers, D. S. & Andrews, B. D., 2014. Assessment of tsunami hazard to the US Atlantic margin, *Mar. Geol.,* **353,** 31–54.

Toda, S., Stein, R. S., Richards-Dinger, K. & Bozkurt, S. B., 2005. Forecasting the evolution of seismicity in southern California: animations built on earthquake stress transfer, *J. geophys. Res.: Solid Earth,* **110**(B5), 1–17.

Tsai, V. C., Hayes, G. P. & Duputel, Z., 2011. Constraints on the long-period moment-dip tradeoff for the Tohoku earthquake, *Geophys. Res. Lett.,* **38**(7). 1–6, doi:10.1029/2011GL049129.

Wells, D. L. & Coppersmith K., J., 1994, New empirical relationships among magnitude, rupture length, rupture width, rupture area, and surface displacement. *Bull Seismol Soc Am,* **84,** 974–1002, doi:10.1785/BSSA0840040974.

Wessel, P., Smith, W. H., Scharroo, R., Luis, J. & Wobbe, F., 2013. Generic mapping tools: improved version released, *Eos, Trans. Am. geophys. Un.,* **94**(45), 409–410.

Yong, C. Z., Denys, P. H. & Pearson, C. F., 2017. Present-day kinematics of the Sundaland plate, *J. appl. Geod.,* **11**(3), 169–177.

Yun, S.H. *et al.*, 2015. Rapid damage mapping for the 2015 M w 7.8 Gorkha earthquake using synthetic aperture radar data from COSMO–SkyMed and ALOS-2 Satellites, *Seismol. Res. Lett.,* **86**(6), 1549–1556.

Zhu, L. & Helmberger, D. V., 1996. Advancement in source estimation techniques using broadband regional seismograms, *Bull. seism. Soc. Am.,* **86**(5), 1634–1641.

SUPPORTING INFORMATION

Supplementary data are available at *GJI* online.

Figure S1. The BMKG seismic stations (green inverted triangles) which recorded the foreshock, main shock (red star) and aftershock events.

Figure S2. An empirical formula that approximates the radius of influence of an earthquake (Herring *et al.* 2016) estimates that coseismic offsets of $^{3}1$ mm will be detected by GPS stations within ∼107 km from the Mamuju mainshock's epicentre location (red star).

Figure S3. Daily GPS time-series in CMJN station spanning a month before and a month after the Mamuju earthquake. Green dots are data we used to estimate the coseismic offsets, blue dots are deleted outlier data and red lines are the model.

Figure S4. Daily GPS time-series in CMJU station spanning a month before and a month after the Mamuju earthquake. Green dots are data we used to estimate the coseismic offsets, blue dots are deleted outlier data and red lines are the model.

Figure S5. Daily GPS time-series in CTOR station spanning a month before and a month after the Mamuju earthquake. Green dots are data we used to estimate the coseismic offsets, blue dots are deleted outlier data and red lines are the model.

Figure S6. Interferograms of the Mamuju earthquake recorded no obvious surface deformation related to the main shock event. (a) Sentinel-1 SAR scenes (2021 January 10 and 22 January). (b) ALOS-2 SAR scenes (stripmap imaging mode, 2020 April 14 and 2021 January 19).

Figure S7. Teleseismic slip inversion results based on the west-dipping fault. (a) and (b) Coseismic slip distribution with a maximum slip of ∼90 cm at a depth of ∼12 km. The red star is the hypocentre location. (c) A moment-rate function for the coseismic slip distribution. (e) A variety of rupture velocities tested for the slip inversion. The preferred rupture velocity (3.0 km s^{-1}) is marked as a blue circle.

Figure S8. Teleseismic waveform fits based on the west-dipping fault. Data (black) and synthetic (red) waveforms are filtered to 0.5 Hz for *P* wave and to 0.2 Hz for *SH* wave. Each waveform is labelled with station code, type of seismic wave and station azimuth. (b) Stations distribution with *P*- and *SH*-wave data used for the inversion.

Figure S9. A misfit function plot for the east-dipping fault. (a) A misfit function plot for the longitude and latitude of the fault. (b) A misfit function plot for the depth (upper left corner) of the rectangular fault. Red symbol represents the longitude, latitude and depth which result in the lowest misfit value.

Figure S10. A misfit function plot for the west-dipping fault. (a) A misfit function plot for the longitude and latitude of the fault. (b) A misfit function plot for the depth (upper left corner) of the rectangular fault. Red symbol represents the longitude, latitude and depth which result in the lowest misfit value.

Figure S11. Coulomb stress changes calculated using our coseismic slip distribution (source) at the location of the 40°-dipping secondary fault (receiver). (a) The result shows that while ∼50 per cent of the aftershock events are within ≥ 10 kPa Coulomb stress changes (green line), the remaining aftershock events are within the negative Coulomb stress changes. (b) An east–west profile that shows the foreshock (square), aftershock (circle) events, the source and receiver faults.

Figure S12. Second invariant rates based on the method of Hackl *et al.* (2009), where GPS velocities are interpolated into a grid size of 0.5°. We masked out the second invariant outside the GPS velocities coverage to avoid overinterpreting artefacts due to the interpolation.

Table S1. Focal mechanism solutions of the main shock event.

Table S2. Coseismic GPS offsets (mm) used in this study.

Table S3. Interseimic GPS velocities (mm yr^{-1}) used in this study.

Please note: Oxford University Press is not responsible for the content or functionality of any supporting materials supplied by the authors. Any queries (other than missing material) should be directed to the corresponding author for the paper.